MOMENTUM BUDGETS OVER IDEALIZED OROGRAPHY WITH A NONHYDROSTATIC ANELASTIC MODEL

P Héreil and J Stein
Météo-France, Centre National de Recherches Météorologiques
Toulouse, France
philippe.hereil@meteo.fr

Abstract

Numerical simulations of idealized orographic flows are carried out with a nonhydrostatic anelastic model to investigate the interaction between nonlinear orographic effects and the synoptic flow, through in-line calculations of momentum budgets in different domains of variable size representative of a meshgrid of a General Circulation Model.
In the hydrostatic regime, for two-dimensional (2D) breaking mountain waves, the mean flow is decelerated in the vertical between the ground and the theoretical breaking level. In the horizontal, the deceleration of the large-scale flow is uniformly distributed by non-resolved acoustic waves. In the regime of three-dimensional (3D) quasi-symmetrical lee vortices, the large-scale flow is decelerated in a restricted region centered on the wake. When the symmetry of the lee vortices is altered, by a long model integration or by introduction of a perturbation, the flow evolves towards the vortex shedding regime. A very long integration of the model numerically shows the growth and the saturation of the perturbation after 160 units of dimensionless time. Budgets of momentum indicate that vortex shedding significantly enhances the large-scale flow deceleration, still located near the wake. Off-line tests of a drag parameterization show that some adaptations are necessary to improve the prediction of the impact of subgrid-scale orographic effects on the large-scale flow for the investigated idealized configuration.
In the nonhydrostatic regime, for 2D non-breaking trapped lee waves, the pressure drag is enhanced but the mean flow is not decelerated at low levels. In case of 3D non-breaking trapped lee waves, the mean flow is decelerated at low levels.

1. INTRODUCTION

When a stratified air is flowing over an obstacle, gravity waves can develop and propagate vertically. The momentum is extracted from the flow aloft and transported downward to balance the orographic drag generated by the pressure gradient across the mountain. In case of momentum dissipation (e.g. wave breaking), the downward flux of horizontal momentum is divergent and thus decelerates the large-scale flow. Under those circumstances, the impact of the subgrid-scale orography needs to be parameterized in a general circulation model (GCM hereafter) in order to compute a realistic forecast.

The purpose of this paper is to test the basic concepts of current drag parameterizations with a high resolution numerical model where the orographic flow is correctly resolved. To facilitate these tests, the real-flow problem is simplified to an idealized problem of orographic flow containing the essential features of the real flow. The tests are carried out through in-line computation of exhaustive momentum budgets in boxes of variable size. The paper is organized as follows. Section 2 contains a brief summary of the method employed for this analysis of momentum transfers. In section 3, the momentum budget is used to analyze three potential sources of mean-flow deceleration in the hydrostatic regime. In section 4, the study is extended to the impact of nonhydrostatic effects on the large-scale flow through the investigation of typical cases of trapped lee waves (tlw in the following). Conclusions of the study are drawn in section 5.

2. STRATEGY

Momentum transfers in orographic flows are studied through numerical simulations with the non-hydrostatic anelastic model Meso-NH (Lafore et al. 1997) of a stable stratified atmosphere over a bell-shaped Witch of Agnesi mountain defined by

$$h(x,y) = \frac{h_0}{\left(1+\left(\frac{x}{a}\right)^2+\left(\frac{y}{a}\right)^2\right)^{3/2}}, \tag{1}$$

where a and h_0 are respectively the half-width and the maximum height of the obstacle. The aspect ratio R of the obstacle is either infinite (2D orography) or set to unity (3D axisymmetrical obstacle). Incident flow speed (U_0) and Brunt-Väisälä frequency (N_0) are uniform by layers far upstream of the obstacle. The atmosphere is dry, adiabatic, frictionless, non rotating, Boussinesq and inviscid. Under these assumptions, the flow regime is controlled by two dimensionless parameters:

$$\hat{h} = \frac{N_0 h_0}{U_0},\ \hat{a} = \frac{N_0 a}{U_0};$$

$\hat{h}$ measures the importance of the nonlinear effects in the momentum equations while $\hat{a}$ controls the nonhydrostatic effects. In the nonhydrostatic regime, the Scorer (1949) number is an additional parameter which controls the wave propagation. Its variation with height may induce wave trapping in a restricted layer of atmosphere. This simplified configuration allows to recover the main features of a real orographic flow while conserving a minimum set of physical parameters controlling the regime of flow.

Once a given regime of orographic flow is reproduced with Meso-NH, to analyze the momentum transfers between meso scale and synoptic scale, the Meso-NH momentum equations are summed within a box of variable size (L_x, L_y, Z) representative of a meshgrid of a GCM to give the momentum budget equation:

$$\underbrace{\partial_t \overline{\widetilde{\rho_{ref} u}}}_{A} + \underbrace{\overline{\partial_x\left(\widetilde{\rho_{ref} u^2}\right) + \partial_y\left(\widetilde{\rho_{ref} uv}\right)}}_{B} + \underbrace{\overline{\partial_x \tilde{\Phi}}}_{C} + \underbrace{\overline{\rho_s \Phi_s \partial_x h}}_{D} + \underbrace{\overline{\rho_{ref} uw(Z)}}_{E} - \underbrace{\overline{\widetilde{\rho_{ref} \mathcal{F}_x}}}_{F} - \underbrace{\overline{\widetilde{\rho_{ref} \mathcal{N} u_x}}}_{G} = Res_u \tag{2}$$

where $\overline{o} = \int_{-L_x/2}^{+L_x/2}\int_{-L_y/2}^{+L_y/2} o\,dxdy$ and $\tilde{o} = \int_{h(x,y)}^{Z} o\,dz$. As a reference, we assume a mean flow directed along x. In (2), A represents the instantaneous variation of momentum in the box. B corresponds to the difference of momentum flux between the lateral sides of the box. C accounts for the variation of momentum due to the horizontal pressure gradient between the lateral sides of the box. D is the mountain pressure drag, and E is the vertical flux of momentum through the top of the box. Term F accounts for the variation of momentum due to turbulent mixing, and term G represents the discrete form for numerical diffusion and upper relaxation in the Meso-NH momentum equation. Finally, Res_u is the residual term of the budget, which must be small compared to the other terms to have a correct closure. This point has been checked for any budget of momentum presented in this paper. The special in-line calculation allows to easily obtain either an instantaneous budget (i.e. calculated on one model timestep) or a temporally averaged budget. A similar integral budget is built for $\rho_{ref} v$.

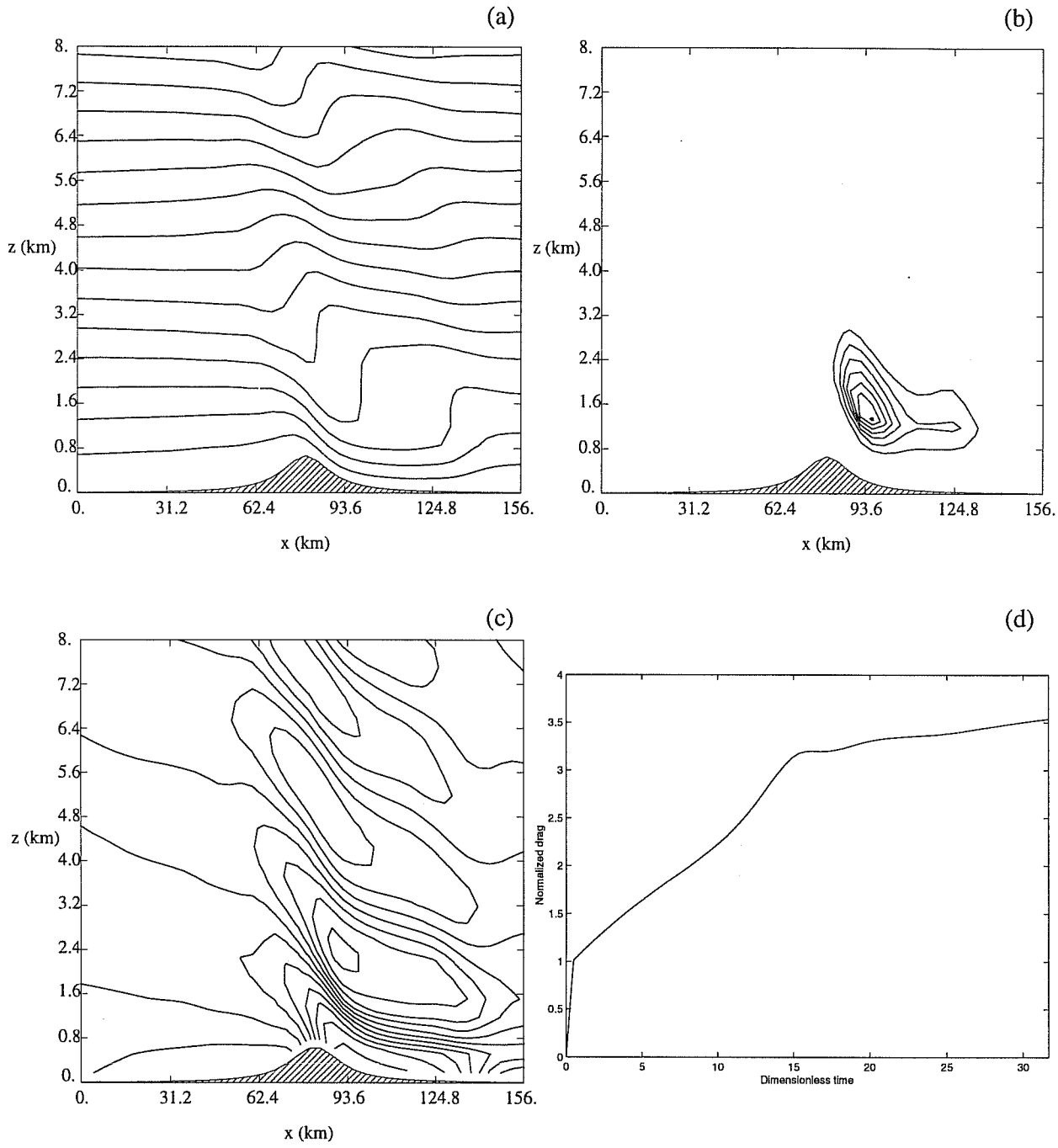

Figure 1: Meso-NH solution for an orographic airflow characterized by $\hat{h} = 1$ and $\hat{a} = 10$: (a) potential temperature (contour interval 2.5 K); (b) Turbulent kinetic energy (contour interval .5 m^2 s^{-2}), (c) horizontal wind (contour interval 2 m s^{-1}) at $t^* = tU_0/a = 32$. In this and in all the figures which follow, the airflow is from left to right. (d) Pressure drag, normalized by D_{lin} as a function of dimensionless time t^*.

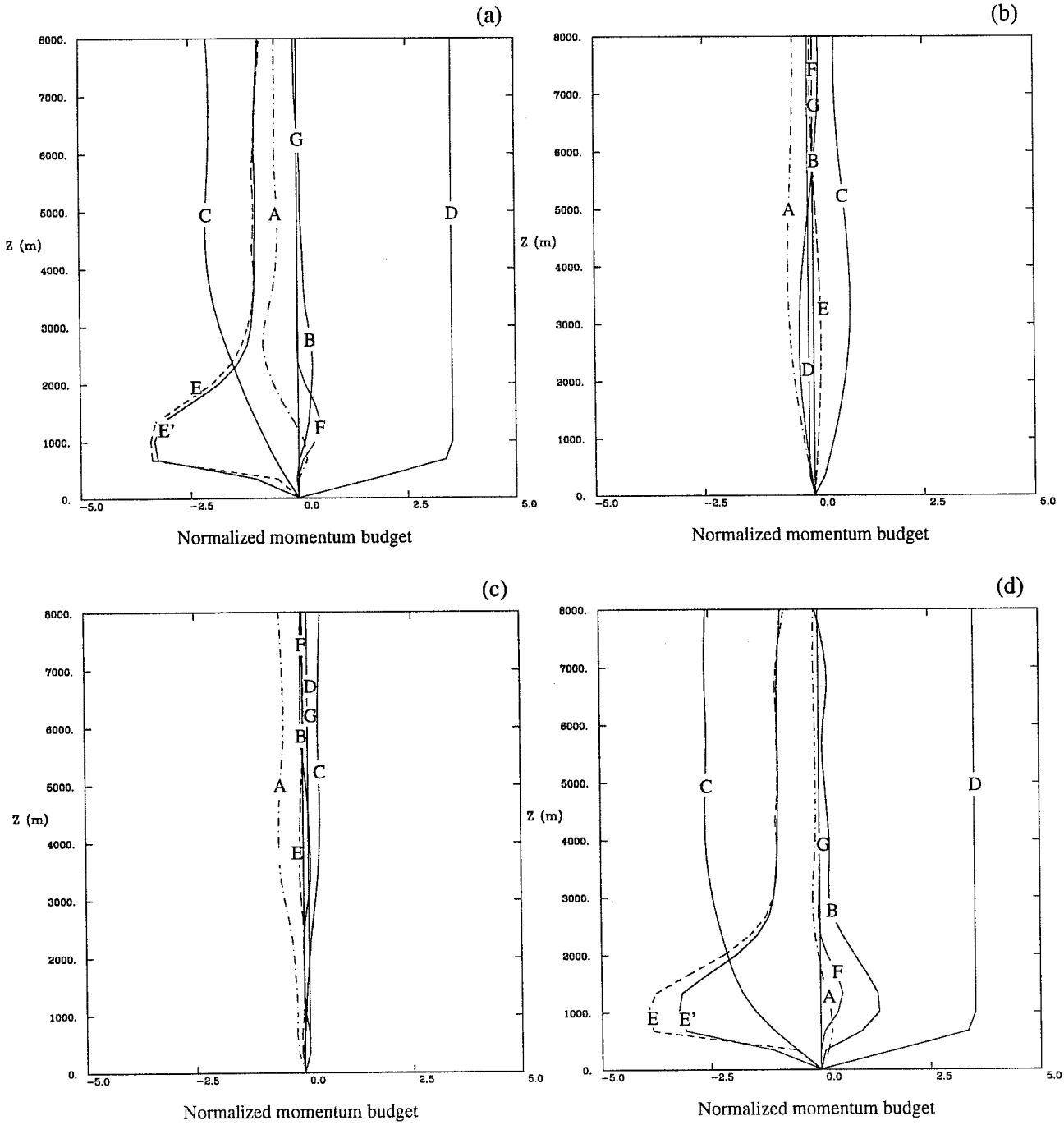

Figure 2: Nonlinear hydrostatic regime ($\hat{h} = 1$, $\hat{a} = 10$): budget of momentum at $t^* = 32$ in a $80a$ wide box (a) centered on the obstacle, (b) localized upstream of the obstacle, (c) localized downstream of the obstacle. The 3 boxes are contiguous. (d) Budget of momentum at $t^* = 32$ in a $14a$ wide box centered on the obstacle. In this and in all the budgets of momentum which follow, all the terms are normalized by the linear theoretical drag D_{lin}.

3. IMPACT OF HYDROSTATIC NONLINEAR EFFECTS ON THE MEAN FLOW

3.1 2D breaking mountain waves

The orographic flow considered here has uniform mean wind speed ($U_0 = 8$ m s^{-1}) and static stability ($N_0 = 0.012$ s^{-1}) far upstream of the obstacle. The mountain is specified by (1), with $R = \infty$. The dimensionless parameters $\hat{h}$ and $\hat{a}$ are respectively 1.0 and 10.0, corresponding to a nonlinear hydrostatic flow. The model is firstly run with cyclic lateral boundary conditions (lbc in the following), and other parameters for this simulation are given in Table 1. Subgrid turbulence is parameterized by the scheme developed by Bougeault and Lacarrère (1989).

	2D breaking mountain waves	lee vortices	2D trapped waves	3D trapped waves
Nx × Ny × Nz	1024 × 1 × 36	120 × 80 × 32	512 × 1 × 80	120 × 80 × 32
Δx	4 km	4 km	1 km	1 km
Δy	/	4 km	/	1 km
Δz	333 m	500 m	200 m	400 m
Δt	60 s	40 s	10 s	10 s
h_0	667 m	3000 m	750 m	750 m
a	10 km	10 km	10 km	10 km
R	∞	1	∞	1
lbc	cyclic	open	open	open

Table 1: Overview of the parameters for the set of numerical simulations.

Initially, the atmosphere is in hydrostatic equilibrium, $u = U_0$ and $N = N_0$. The obstacle is abruptly inserted in the flow, and the model is integrated until $t^* = 32$, leading to the solution displayed in Fig. 1. In the potential temperature field (Fig. 1a), a region of wave breaking is clearly visible just below the theoretical breaking level ($z_c = 0.75\,\lambda_z$, where $\lambda_z = 2\pi U_0/N_0$ is the analytic value of the vertical wavelength for hydrostatic gravity waves). Strong turbulent mixing is associated with breaking (see Fig. 1b). Breaking features are also apparent in the u field reported in Fig. 1c, where exists a zone of reverse flow in altitude, and a windstorm near the ground. In the evolution of the pressure drag (Fig. 1d), we note that after a rapid growth until $t^* = 15$, the drag increases up to 3.5 times its theoretical linear value ($D_{lin} = \pi/4\rho_{ref}U_0N_0h_0^2$) by $t^* = 32$.

In order to study the distribution of the mean-flow deceleration in the physical domain, we have computed the budget of momentum for the model solution at $t^* = 32$ (Fig. 2). The different terms of the budget are defined in (2). The momentum budget is calculated at different locations of the physical domain, in a box of size $80a$, representative of the horizontal extension of a GCM meshgrid. A supplementary term E' defined by

$$E' = \overline{\rho_{ref}u'w'} = \overline{(\rho_{ref}u - \overline{\rho_{ref}u})(w - \overline{w})} = \overline{\rho_{ref}uw} - \overline{\rho_{ref}u}\,\overline{w} = E - \overline{\rho_{ref}u}\,\overline{w} \qquad (3)$$

has been added. E is the exact vertical momentum flux required to close the momentum budget (2). In the conventional scheme where linear mountain waves transport positive momentum downward to exactly balance the pressure drag, the fields perturbations vanish far from the obstacle and $\overline{w} = 0$. In the finite-domain solutions of a time-dependent nonlinear model, $\overline{w}$ is different from 0, and we have

to calculate E' to compare the results with the predictions of the Eliassen and Palm (1960) theorem. E' is the source of deceleration which would exist if the numerical domain was quasi-infinite.

The momentum budget for a box of size $80a$ centered on the obstacle is plotted in Fig. 2a. In this profile, the pressure drag is partly balanced by the vertical flux of horizontal momentum. The decrease (here and in the following, in terms of absolute value) of the vertical flux of momentum is located between the ground and the breaking level z_c, with a magnitude of 2.5 D_{lin}. Above z_c, all the terms are uniform with height, this means that momentum transfers are located below the breaking level. Below z_c, the divergence of the vertical flux of momentum is mainly balanced by the pressure term C and by the tendency term A. When the width of the budget box is extended to the domain limits, the lateral terms (B and C) vanish, due to the imposition of periodic conditions, and the divergence of the vertical flux is entirely balanced by the tendency term. In a periodic domain, the tendency term thus accounts for the deceleration of the mean flow, and the pressure term only acts to distribute the mean-flow deceleration in the physical domain. For this $80a$ box, the tendency term is equal to 20% of the divergence of the vertical momentum flux, and as a consequence, only 20% of the deceleration occurs in this central box. Still in Fig. 2a, it is worth noting the role played by the turbulent term which tends to vertically redistribute momentum, between the ground and z_c. The turbulence acts against the wind shear to restore the original wind profile. Concerning the lateral term B, it redistributes momentum between the ground and the top of the simulation domain.

To specify the horizontal distribution of the mean-flow deceleration, momentum budget has been calculated in 2 boxes of size $80a$, contiguous to the central box, located upstream (see Fig. 2b) and downstream (see Fig. 2c) of the obstacle. If we compare with the previous budget in the central box (see Fig. 2a), the three tendency terms (A) are found to be very close. This implies that the deceleration is equally distributed between the 3 boxes. Budget profiles (not shown) in the remaining $80a$ boxes located at the limits of the domain present the same profile of tendency terms. Thus, the mean-flow deceleration is uniformly distributed in the horizontal. Looking at Fig. 2a, one can see that this is the pressure term which distributes uniformly the mean-flow deceleration. Further analysis shows that when exists a variation of momentum in the model in a 2D configuration, the pressure solver uniformly distributes this variation in one timestep by creating an adequate pressure gradient.

Momentum budget calculation in a narrow box ($L = 14a$) centered on the obstacle (see Fig. 2d) shows that the source of deceleration for the whole numerical domain, i.e. the divergence of the vertical flux of horizontal momentum E', is fully constructed on a few mountain half-widths.

To reproduce the conditions of an infinite domain with a reasonable computing cost, it is interesting to replace periodic lbc by open conditions. In order to study the impact of lbc on the mean-flow deceleration, we have run again the previous case with open lbc. In Fig. 3 is displayed the evolution of the domain-averaged momentum as a function of time for both simulations. This quantity is defined by

$$< \rho_{ref} u >= \frac{1}{W} \int_{-W/2}^{+W/2} \int_{h}^{H} \frac{\rho_{ref} u}{H-h} dx dz,$$

where H and W are respectively the height and the width of the full numerical domain. As it can be

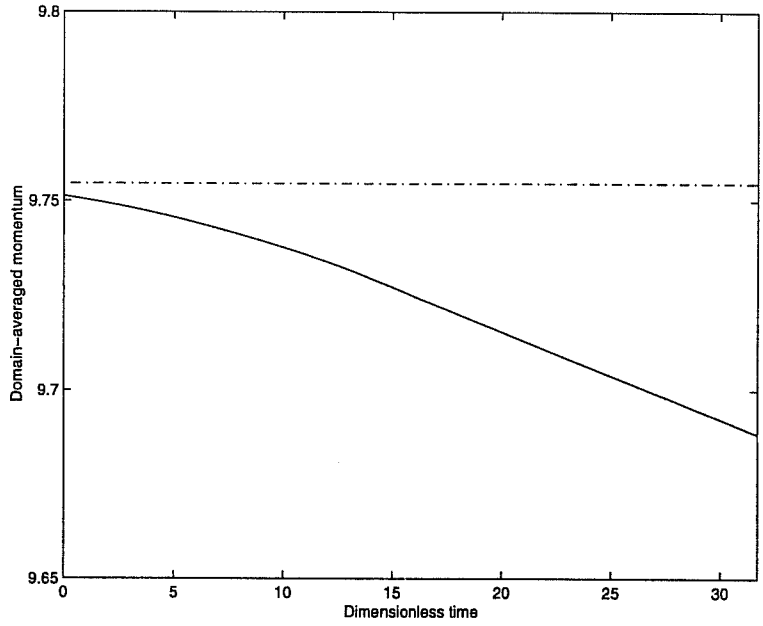

Figure 3: Meso-NH solution for an orographic airflow characterized by $\hat{h} = 1$ and $\hat{a} = 10$: domain-averaged momentum (kg m^{-2} s^{-1}) as a function of dimensionless time t^* for the simulation with open lbc (dash dot) and for the simulation with periodic lbc (solid line).

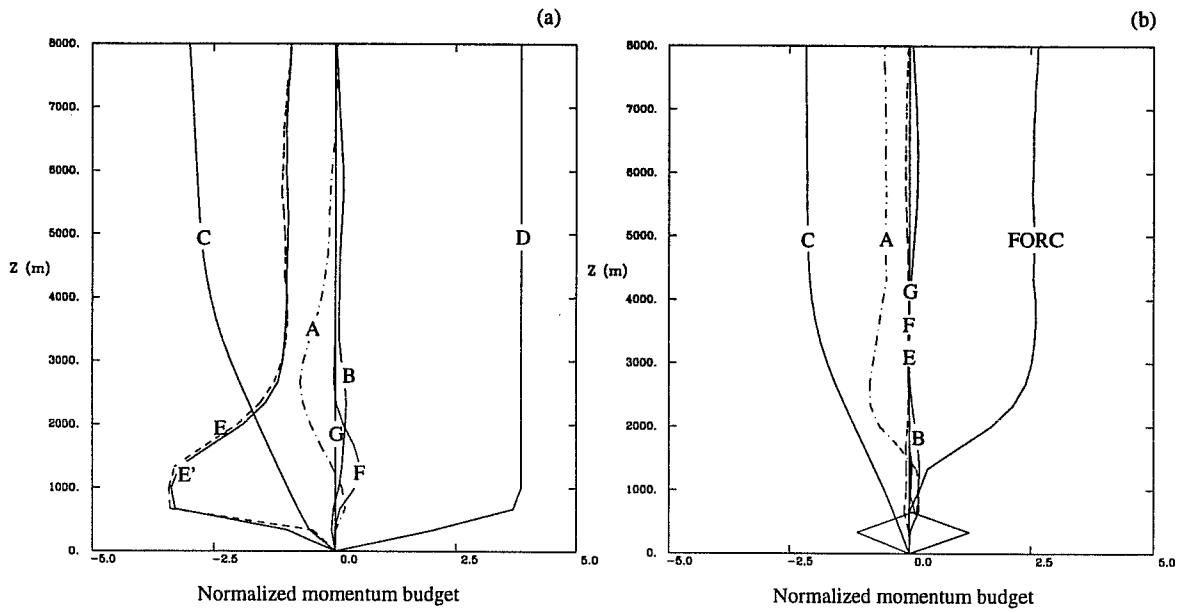

Figure 4: (a) Meso-NH simulation with open lbc of the nonlinear hydrostatic regime ($\hat{h} = 1$, $\hat{a} = 10$): budget of momentum at $t^* = 32$ in a $80a$ wide box centered on the obstacle. (b) Simulation with a large-scale model (cyclic lbc) without orography, and forced by the divergence of the vertical flux of momentum of the meso-scale model: budget of momentum at $t^* = 32$ in a $80a$ wide box centered on the obstacle.

seen in Fig. 3, global momentum is nearly uniform for the simulation with open lbc while it linearly decreases for the simulation with periodic lbc. Open lbc therefore conserve global momentum in the simulation domain. As a consequence, the mean flow cannot be decelerated in the whole simulation domain with open lbc.

In order to verify this statement, the budget of momentum has been calculated for the simulation with open lbc (Fig. 4a), for the same central box as for the periodic case (see Fig. 2a). Comparison between both budget profiles reveals that the tendency term (A) decreases dramatically, and even vanishes at the top of the domain with open lbc. In this upper region, the vertical momentum flux divergence is entirely balanced by an increase of the pressure term. Open lbc have created a supplementary horizontal pressure gradient which prevents the mean-flow deceleration at any place extending vertically up to the top of the simulation domain.

The Meso-NH model is now used to simulate the response of a GCM to a parameterized orographic forcing. The low-resolution model is integrated in a limited cyclic area defined by 32 horizontal grid points with a 128-km mesh interval and with 36 layers of 333-m depth each. Other model parameters are as before, excepted for orography, which is removed. To reproduce the effect of the subgrid-scale orography, a forcing ($D + E$ of the meso-scale model) is introduced in the GCM. The GCM is integrated until $t^* = 32$, and the budget of momentum is calculated for a 7-point wide box. When we compare the corresponding budget profile (Fig. 4b) to its counterpart calculated with the wave-resolving model (Fig. 2a), there is a good accordance between the tendency and pressure terms. Thus, when it is well parameterized, the vertical flux of momentum is the only term required by a GCM to accurately reproduce the mean-flow deceleration existing in a meso-scale anelastic model for this case of breaking mountain waves, and there is no need to parameterize additional budget terms to obtain a realistic behaviour of the GCM.

As the consideration of a 2D orographic flow may be too restrictive compared to the dynamics of a real orographic flow where 3D nonlinear effects play an important role, the study is now extended to the interaction of 3D nonlinear orographic effects with the large-scale flow.

3.2 3D lee vortices

The 3D orographic flow considered here has been numerically simulated by Schär and Durran hereinafter referred to as SD97). The mountain is defined by (1) with $h_0 = 3$ km, $R = 1$, $a = 10$ km, and is located at the origin of the coordinate system. The atmosphere has uniform mean wind speed ($U_0 = 10$ m s^{-1}) and static stability ($N_0 = .01$ s^{-1}) far upstream of the obstacle. Under these conditions, the dimensionless parameters are $\hat{h} = 3.0$ and $\hat{a} = 10.0$, and the flow belongs to the hydrostatic non-linear regime. In the numerical model, the incident flow is aligned with the positive x-axis and lbc are open. Other parameters are given in Table 1. At the contrary of the SD97 numerical simulation, the model solution is not here forced to be symmetrical.

The Meso-NH solution at $t^* = 40$ is presented in Fig. 5. In a vertical section along the center plane of the horizontal wind field (Fig. 5a), one can observe the coexistence of a pronounced upstream

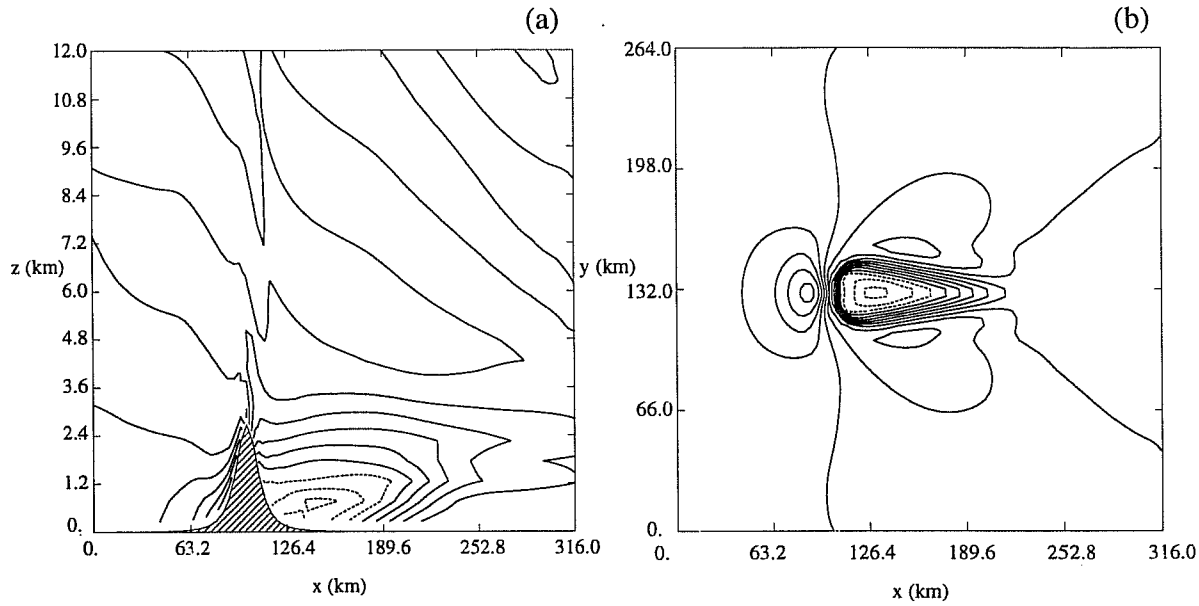

Figure 5: Meso-NH solution at $t^* = tU_0/a = 40$ for an orographic airflow characterized by $\hat{h} = 3.0$ and $\hat{a} = 10.0$: (a) horizontal wind field u (contour interval 2 m s^{-1}) in a vertical section along the center plane, (b) horizontal wind field u (contour interval 2 m s^{-1}) at the surface. Negative values are plotted in dashed lines. In these figures, and in the following, the airflow is from left to right, oriented parallel the x direction.

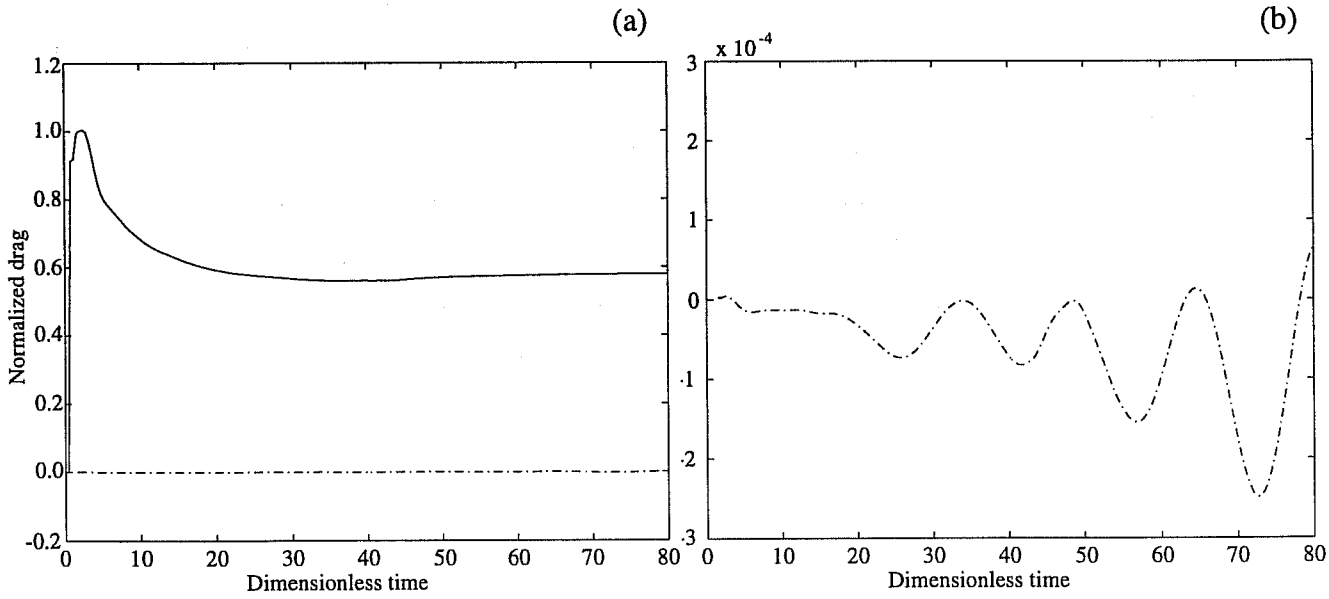

Figure 6: Meso-NH solution for an orographic airflow characterized by $\hat{h} = 3.0$ and $\hat{a} = 10$: pressure drag, normalized by D_{lin}, as a function of dimensionless time $t^* = tU_0/a$. (a) Solid line and dash-dot line respectively represent the along-flow component (x) and the cross-flow (y) component of the drag; (b) enlargement of the evolution of the cross-flow component of the drag.

deceleration (minimum value of .2 U_0) with an elongated reverse flow downstream (minimum value of -.6 U_0) nearly stationary by $t^* = 40$. In the horizontal wind field at the surface (Fig. 5b), one can see that the reverse flow is associated with two contra-rotative quasi-symmetrical lee vortices.

An overview of the drag evolution is provided in Fig. 6. The along-flow (x) component of the drag (Fig. 6a) tends towards a nearly steady state after $t^* = 20$, characterized by an amplitude of .6 D_{lin}. $D_{lin} = .25\pi\rho_{ref}U_0N_0ah_0^2$ is the hydrostatic linear drag value for an axisymmetrical obstacle (Phillips 1984). The cross-flow (y) component of the drag (Fig. 6b) has an amplitude 3 orders of magnitude smaller than the along-flow component. Nevertheless, from $t^* = 20$, it exponentially amplifies with time (growth rate equal to 0.03), with a pseudo-period estimated to $T^* = 15$. This evolution indicates that the flow progressively becomes asymmetrical, despite an axisymmetrical obstacle exactly centered in the simulation domain.

In the 2D numerical experiments described previously, it has been shown that open lbc involve the conservation of the global momentum in the simulation domain. In order to study if this problem still exists for 3D simulations, the evolution of global momentum in the 3D numerical domain has been calculated for simulations employing different lbc: cyclic, open and wall (see Fig. 7). As one can see, the association of open-wall lbc exclusively involves the conservation of global momentum. The other 3D associations lead to a decrease of global momentum. Thus, 3D open lbc exert no constraint on global momentum, due to the presence of a supplementary degree of freedom on v in the anelastic equation of the 3D model. As all the 3D orographic flows of the present paper are simulated in an open simulation domain, the tendency term calculated in the 3D momentum budget can be considered as a good diagnosis of the distribution of the mean-flow deceleration.

In order to study the interaction between the orographic flow and the large-scale flow, the budget of $\rho_{ref}u$ has been calculated for the model solution at $t^* = 40$. Because of the oscillation of the solution with time (see the y component of the drag in Fig. 6b), the budget has been averaged over one period of oscillation ($T^* = 15$). The lateral terms B and C are associated in (2) in a single term denoted $B + C$, in order to facilitate the budget analysis. Furthermore, term $(B + C)'$ is added to describe the budget in a quasi-infinite budget box. It is defined by (B+C)' = (B+C) - (E-E'). In the budget profile (Fig. 8a), the loss of momentum due to pressure drag is mainly balanced by the vertical flux of horizontal momentum, the tendency term and the lateral term. The vertical flux E' is strongly divergent between the ground and the mountain top h_0, and never balances the drag in the low levels (at the contrary of the 2D case of breaking mountain waves). The effective divergence of the vertical flux is equal to the departure of the flux from its profile balancing the drag. The decrease of the vertical flux is found to be equal to $.4D_{lin}$, and represents the potential source of mean-flow deceleration. Above h_0, the flux divergence is less intense, and corresponds to the slow construction of the vertical flux. This feature has been confirmed by model integration until $t^* = 80$. The residual flux only balances 20% of the drag at $z = h_0$. The remaining of the drag is balanced by the tendency term (20%) and by the lateral term (60%). According to the previous conclusions concerning the role of lbc, the tendency term represents the local mean-flow deceleration in the box where the budget is

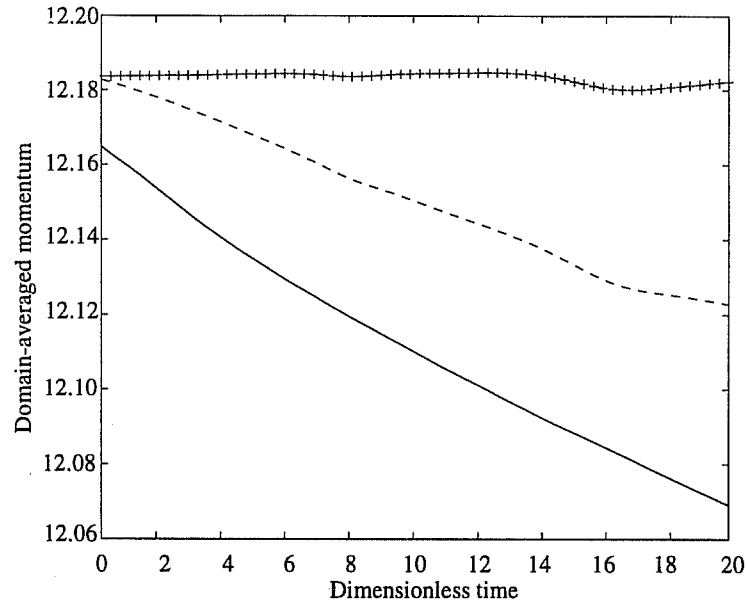

Figure 7: Lee vortices regime ($\hat{h} = 3$, $\hat{a} = 10$): domain-averaged momentum (kg m^{-2} s^{-1}) as a function of dimensionless time t^* for simulations with different lbc: open (dashed line), cyclic (solid), open in one direction, wall in the other (cross).

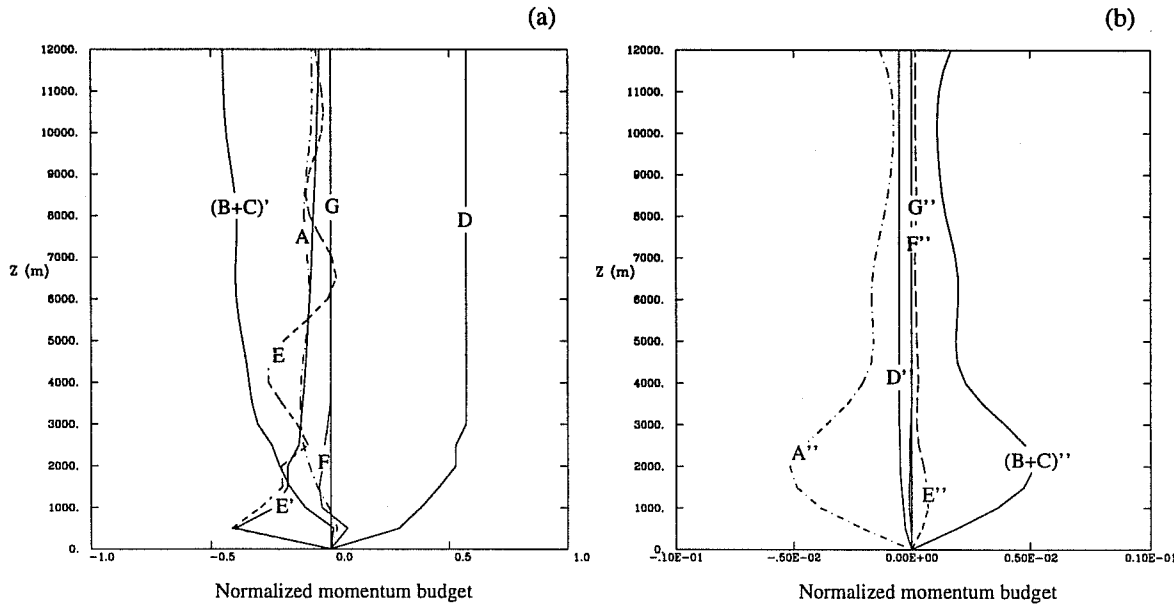

Figure 8: Lee vortices regime ($\hat{h} = 3$, $\hat{a} = 10$): time-averaged budget of momentum at $t^* = 40$ in a box ($L_x = 40a$, $L_y = 30a$) centered on the obstacle. (a) Budget of $\rho_{ref}u$; (b) budget of $\rho_{ref}v$. The average period is set to $T^* = 15$.

computed. It is worth noting that 3D nonlinear effects associated with flow splitting concentrate the mean-flow deceleration below the mountain top.

The budget of $\rho_{ref}v$ momentum leads to terms which are two orders of magnitude smaller than the terms of the budget of $\rho_{ref}u$ (see Fig. 8b). As a consequence, the $\rho_{ref}v$ momentum has a negligible contribution to the global momentum transfer in the lee-vortices regime.

In order to study the horizontal distribution of the mean-flow deceleration, the tendency $(\partial_t \rho_{ref} u)$ has been computed in the whole numerical domain. In the vertical section along the center plane (Fig. 9a), a zone of negative tendency (deceleration) is clearly visible downstream. In the vertical, this zone is located below the mountain top, in accordance with the previous analysis of the momentum budget. In the tendency field at $z = 0.5\ h_0$ (Fig. 9b), one can see that negative values are distributed in either flank of the wake, while positive values are found in a more restricted area located in the core of the wake. It is worth noting that the tendency field is not perfectly symmetrical, which is another evidence of the progressive transition of the symmetrical vortex regime towards the vortex shedding regime. The tendency field thus indicates that most of the mean-flow deceleration at $t^* = 40$ is concentrated in a restricted area including the wake. Computation of the tendency term A of the $\rho_{ref}u$ budget in this restricted region leads to the profile reported in Fig. 9c. As it can be seen, this term is equal to 80 % of the tendency term in the large box (compare with Fig. 8a). This result confirms that most of the mean-flow deceleration at $t^* = 40$ is preferentially exerted in the restricted area including the wake, and validates the use of the tendency field as a diagnosis of the mean-flow deceleration in a given box.

In order to study the evolution of the mean-flow deceleration, the momentum budgets and the tendency field have been computed at $t^* = 80$. As it can be seen in the budget profile computed in the large box (Fig. 9d), the main difference with the budget at $t^* = 40$ is the decrease of the tendency term. This decrease is compensated by an increase of the lateral term $(B + C)'$, the other budget terms being unchanged. Thus, the mean-flow deceleration is continually advected at the exterior of the numerical domain during the simulation.

3.3 Transition to vortex shedding

In order to accelerate the loss of symmetry previously observed in the regime of lee vortices, an asymmetrical perturbation of potential temperature (with a maximum amplitude of 3 K) has been introduced in the model solution of quasi-symmetrical lee vortices at $t^* = 40$, then the model freely evolves. The model solution at $t^* = 160$ is displayed in Fig. 10. This long time of integration is required to study the evolution of the y component of the pressure drag. In a vertical section along the center plane of the horizontal wind field (Fig. 10a), successive patches of decelerated flows are visible downstream of the obstacle, and reveal the flow transition to the vortex shedding regime. Recirculation occurs very close from the obstacle, with a minimum velocity of $-.2U_0$. In the vertical, the gravity wave activity has been enhanced by the flow transition. In the horizontal wind field near the ground (Fig. 10b), one can observe that regions of decelerated flow are flanked by alternative

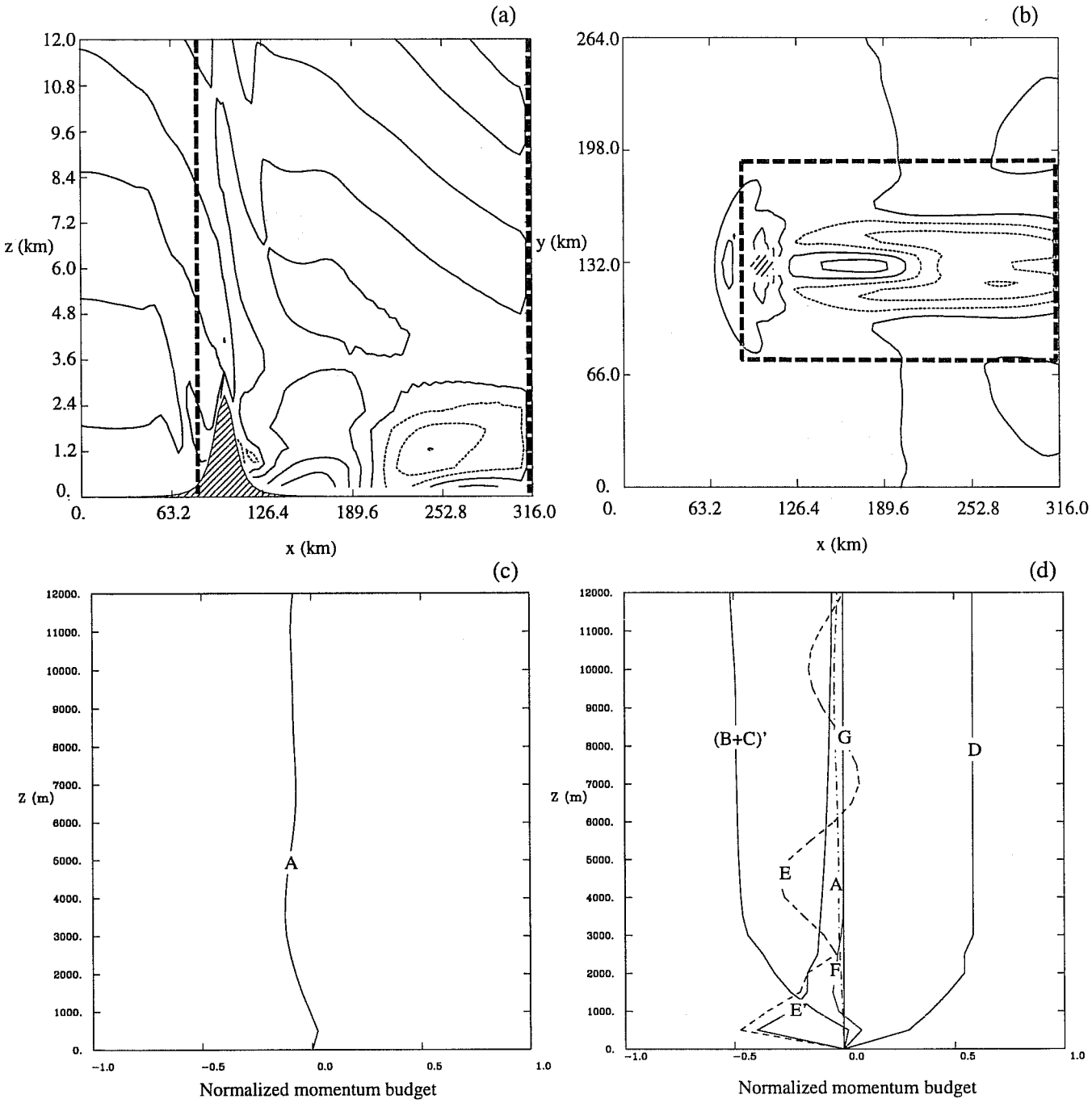

Figure 9: Lee vortices regime ($\hat{h} = 3$, $\hat{a} = 10$): time-averaged tendency (contour interval 5. 10^{-5} kg m^{-2} s^{-2}) (a) at $z = h_0/2$; (b) in a vertical section along the center plane. The period of average is set to $T^* = 15$. Negative values are plotted in dashed lines. (c) Tendency term of the time-averaged budget of $\rho_{ref}u$ calculated in the downstream box indicated by large dashes in (a) and (b). (d) time-averaged budget of $\rho_{ref}u$ at $t^* = 80$ in a box ($L_x = 40a$, $L_y = 30a$) centered on the obstacle.

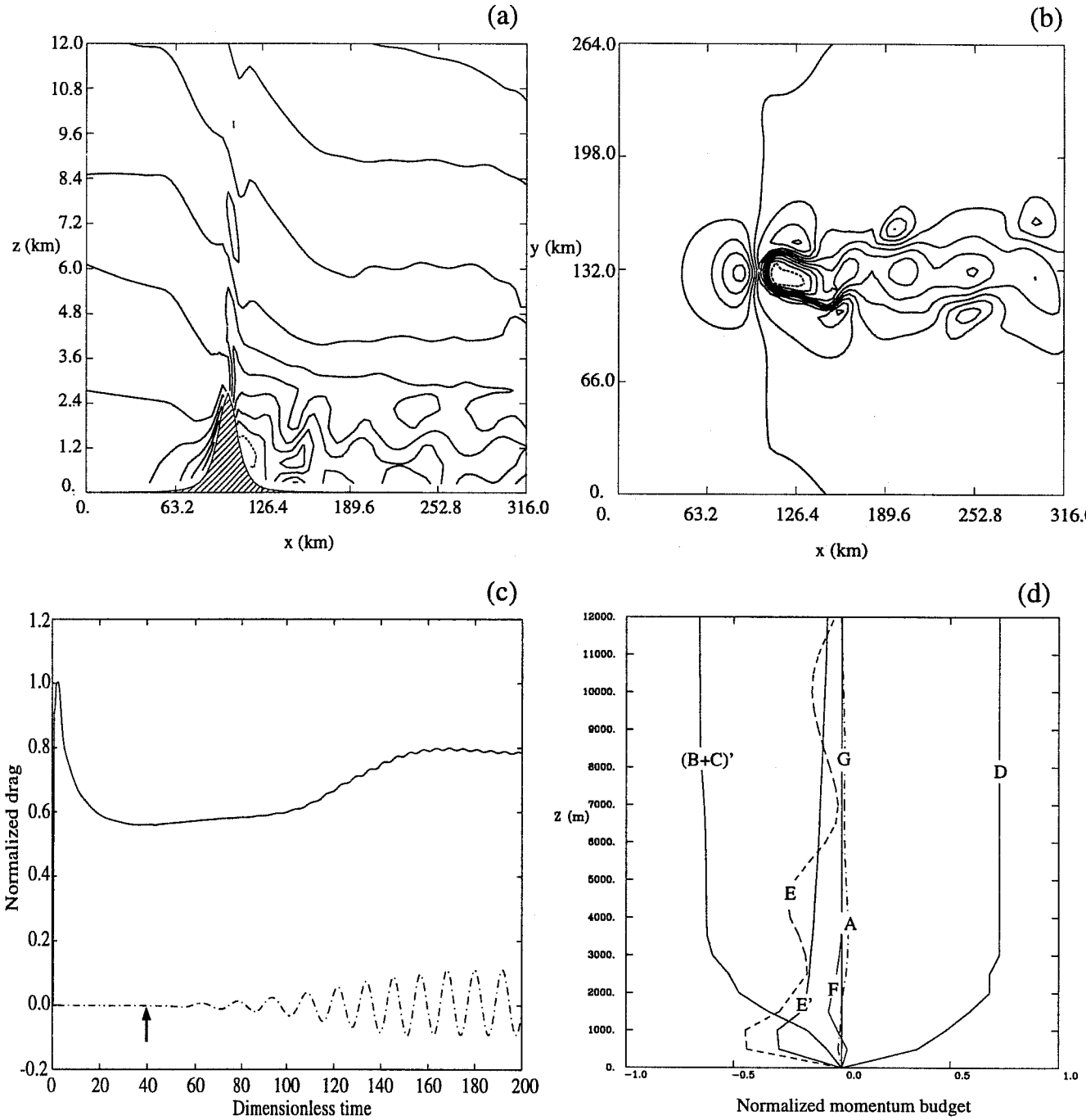

Figure 10: Meso-NH solution at $t^* = tU_0/a = 160$ for the perturbed airflow ($\hat{h} = 3.0$, $\hat{a} = 10.0$): (a) horizontal wind field u (contour interval 2 m s^{-1}) in a vertical section along the center plane, (b) horizontal wind field u (contour interval 2 m s^{-1}) at the surface. Negative values are plotted in dashed lines. (c) Pressure drag, normalized by D_{lin}, as a function of dimensionless time t^*. Solid line and dash-dot lines respectively represent the x component and the y component of the drag. The time when the perturbation has been introduced is indicated by an arrow. (d) Time-averaged budget of $\rho_{ref}u$ at $t^* = 160$ in a box ($L_x = 40a$, $L_y = 30a$) centered on the obstacle. The time-average interval is set to $T^* = 12$.

patches of accelerated flow. This structure oscillates in time with a period $T^* = 12$.

As it can be seen in the temporal evolution of the drag reported in Fig. 10c, the x component of the drag increases up to .8 D_{lin} at $t^* = 160$, and then is quite constant. In Fig. 10c, one can note that the y component of the drag oscillates and amplifies in time until $t^* = 160$, with again a period $T^* = 12$. This evolution is the signature of the growth of a perturbation with time. Further analysis shows that the y component exponentially amplifies in time, proportionally to $e^{0.03t^*}$. After $t^* = 160$, the amplitude of the cross-flow component saturates at $.1D_{lin}$. The maintenance of the perturbation in the lee of the obstacle corresponds to an absolute instability, according to the criterion stated by Huerre and Monkewitz (1990). It must be pointed out that the rounding errors of the calculator have played here the role of the inhomogeneities which lead vortices to shed in a real flow. Finally, comparison of these results with the instability reported in the previous case of quasi-symmetrical lee vortices indicates that the flow transition to the vortex-shedding regime occurs in the initially symmetrical solution, provided the time of integration is long enough, or/and the initial perturbation has a sufficiently large amplitude.

In order to study how the transition to vortex shedding may modify the large-scale flow, the budget of momentum has been calculated in a box of size ($40a$,$30a$) centered on the obstacle (Fig. 10d). Compared to the quasi-symmetrical regime (see Fig. 8a), the budget presents the same general features. The increase of the wave activity in case of vortex shedding does not seem sufficient to modify the vertical flux of momentum. The essential difference between both budgets is the drag enhancement (+35%) induced by the vortex-shedding regime. As the vertical flux has the same profile for both regimes, the drag enhancement due to the transition to vortex shedding therefore involves an increase of the mean-flow deceleration.

For the case of 2D breaking mountain waves, it has been found that the divergence of the vertical flux of momentum is the essential forcing that a drag parameterization must provide to a GCM. It is now interesting to test if a current drag parameterization is able to accurately reproduce this essential forcing for a typical orographic flow in the nonlinear regime. The off-line prediction of the Lott and Miller (1997, in the following LM97) parameterization is reported in Fig. 11. The foreseen vertical flux is divergent between the ground and $z = 4000$ m. The total flux decrease is largely overestimated (more than twice the model value), and the height of interaction is 1000 m higher than for the numerical model. Further analysis has shown that this difference is due to the overestimation of the flux near the ground by the linear part of the scheme (-1.2D_{lin}). The blocked-flow part of the scheme is only active between the ground and the blocked height ($z = 2500$ m), resulting in a flux variation of $.2D_{lin}$. In this region, the linear part of the flux is uniform with height. Above the blocked height, the saturation principle is activated and involves a strong divergence of the vertical flux below the level $z = 4000$ m. As the present parameterization is suited to real synoptic flows where other momentum sinks exist (surface friction for instance), the prediction is not optimal for this idealized free-slip case of 3D lee vortices.

After the analysis of three typical orographic flows in the nonlinear hydrostatic regime, the study

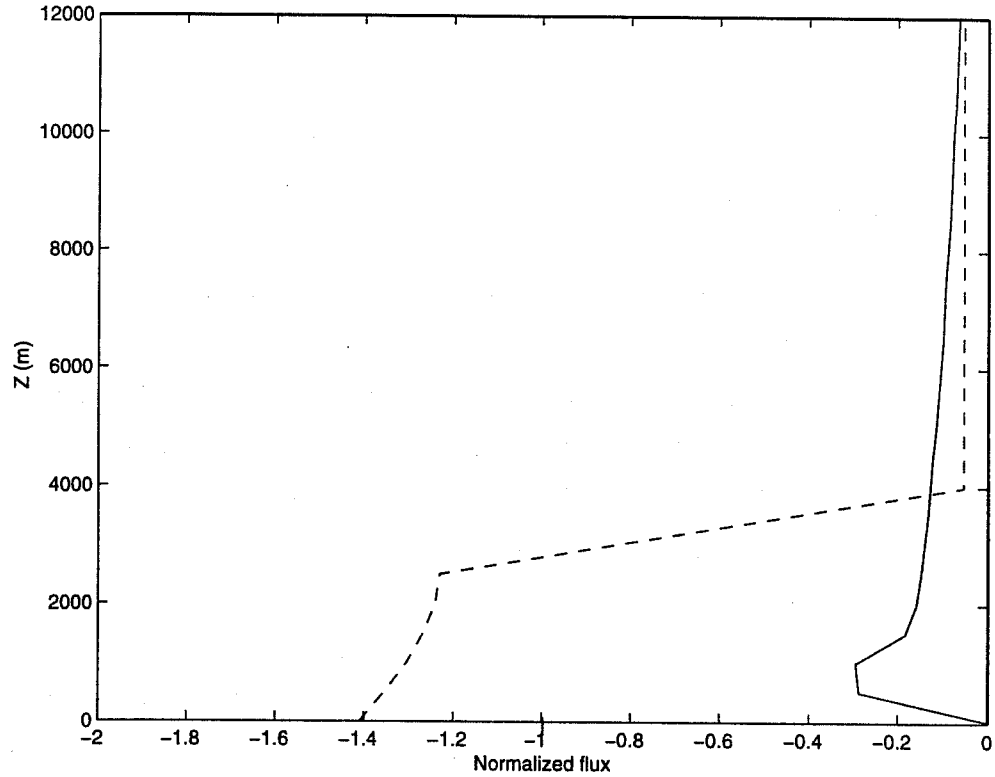

Figure 11: Profiles of vertical flux foreseen by the LM97 parameterization (dashed line) and found by the numerical model (solid line) for the case of 3D lee-vortices.

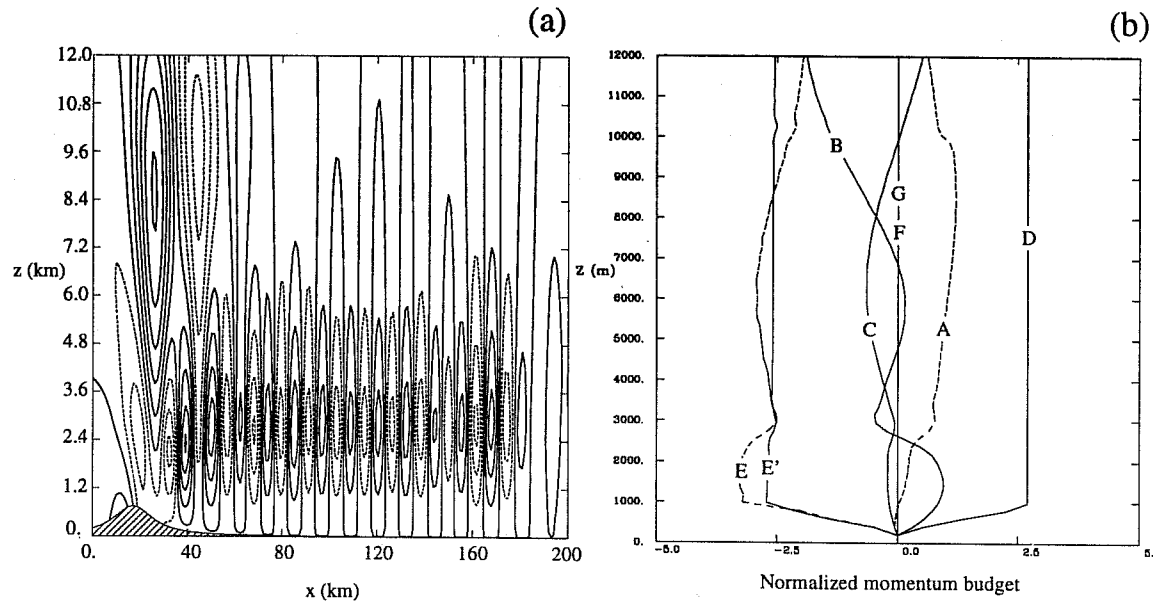

Figure 12: Meso-NH simulation of 2D trapped lee waves: (a) vertical wind (contour interval .4 m s^{-1}) at $t^* = 30$. (b) Budget of momentum in a $40a$ wide box centered on the obstacle.

is now extended to the influence of nonhydrostatic effects on the mean-flow deceleration, through the numerical investigation of idealized tlw.

4. IMPACT OF NONHYDROSTATIC NONLINEAR EFFECTS ON THE MEAN FLOW

4.1 2D trapped lee waves

The interaction of nonhydrostatic effects with the mean flow is now investigated through the Meso-NH simulation of a typical event of 2D non-breaking tlw described by Durran (1995, in the following D95). The basic flow has a wind speed which linearly increases from 10 m s^{-1} at the surface to 40 m s^{-1} at $z = 10$ km, and remains uniform above this height. An inversion layer is located in the region $2.1 < z < 3.1$ km, with a maximum Brunt-Väisälä frequency of .02 s^{-1}. Below this layer, $N = .005$ s^{-1}, and above the inversion, $N = .01$ s^{-1}. The mountain is defined by (1), with $h_0 = 750$ m, $a = 10$ km and $R = \infty$. With dimensionless parameters near the ground equal to $\hat{a} = 5.0$ and $\hat{h} = 0.4$, the orographic flow belongs to the nonlinear nonhydrostatic regime. Turbulent mixing is absent, and additional parameters for this simulation are given in Table 1.

The Meso-NH solution at $t^* = 30$ is reported in Fig. 12a. Vertical wind field shows the superposition of a hydrostatic wave, propagating aloft, with tlw propagating downstream, and having a maximum amplitude located near the inversion layer. The wavelength of the horizontally propagating waves is $2\pi U_0/N_0$. Furthermore, the wave train propagates downstream at a speed of 8.5 m s^{-1}, in agreement with the phase speed of tlw calculated by Nance (1995).

For this regime of non-breaking tlw, momentum budget has been calculated in a $40a$ box centered on the obstacle. As non linearities involve unsteadiness of tlw (Nance 1995), the budget calculation has been averaged on 100 timesteps, which corresponds to the oscillation period of these waves. The corresponding budget is displayed in Fig. 12b, where the normalization constant ($.03h_0^2$) is the value of the drag determined by a numerical simulation of the same case with a reduced mountain height. As it can be seen in this budget profile, the normalized drag is equal to 2.5: trapping significantly enhances the drag. The loss of momentum due to pressure drag is balanced by an uniform vertical flux E'. This exact balance involves that the 2D tlw simulated here do not significantly modify the conventional transport of momentum by vertically propagating mountain waves.

If 2D tlw seem inefficient to modify the conventional scheme of momentum transfer, it cannot be excluded that non Boussinesq effects lead the primary vertically propagating wave to break in the stratosphere. As the drag computed for this case of breaking waves represents, in terms of physical units, the third of the drag determined for the case of breaking mountain waves, 2D tlw may have an important impact on the mean-flow deceleration in altitude, and must be taken into account in a parameterization of subgrid-scale orographic effects.

4.2 3D trapped lee waves

The atmospheric profiles of mean stratification and wind are the same as for the 2D experiment, but the obstacle has a 3D shape defined by (1) with R =1. An overview of the model parameters

employed for this simulation is provided in Table 1. As it can be seen in the Meso-NH solution of w at $t^* = 30$ (cf Fig. 13a), mountain waves essentially propagate downstream of the obstacle, with an horizontal wavelength equal to 12 km. This nonhydrostatic propagation is caused by the trapping of the waves in the layer of stronger stratification. In return, if the 3D tlw pattern is extending downstream with time, the wave amplitude decreases downstream following the law $1.6r^{-.5}$ (r is the radial distance distance from the obstacle). In the horizontal section of the w field at $z = z_i = 3$ km (Fig. 13b), one can observe the superposition of a transverse wave with a diverging wave. Using the analogy with ship waves, as proposed by Sharman and Wurtele (1983), it is possible to determine the theoretical angle θ_1 containing the wedge. The predicted angle is reported in the w field, and as it can be observed, the wedge is mainly contained within the theoretical angle.

The budget of $\rho_{ref}u$ has been calculated at $t^* = 30$, in a box of size ($6a$,$5a$), leading to the profile displayed in Fig. 14. To limit the oscillations of the budget terms due to the presence of nonstationarities, the momentum budget has been temporally averaged over one period of oscillation of the x component of the drag. In the corresponding budget, the vertical flux of momentum E' mainly decreases ($.3D_{lin}$) between $z = 1000$ m and the level $z_i = 3000$ m where static stability is maximum. Between z_i and the top of the physical domain, the flux progressively decreases to $.4D_{lin}$, resulting in a global decrease of $.5D_{lin}$. Calculation of momentum budget at $t^* = 20$ (not shown) indicates that the maximum divergence of the vertical flux is due rather to nonhydrostatic 3D effects than to the slow construction of the flux. Concerning the other terms of the budget at t^* = 30 (Fig. 14), they oscillate with the height of the budget box, due to the proximity of the wave field imposed by the small meshgrid employed in this strongly nonhydrostatic simulation. These oscillations vanish when the budget is calculated in a very large box, which would require a very time-consuming simulation. As a consequence, it has not been possible to determine the distribution of the mean-flow deceleration in the horizontal from the tendency term. Nevertheless, the present budget shows the existence of a source of mean-flow deceleration in the low levels. The decrease of the amplitude of 3D tlw, more pronounced than for 2D tlw, could be responsible for the mean-flow deceleration by preventing the transport of the large-scale flow deceleration far from the obstacle.

5. CONCLUSIONS

This numerical study of different idealized orographic flows with a nonhydrostatic anelastic model has permitted to recover or to identify different mechanisms affecting the mean flow in the context of an idealized problem of nonlinear orographic flows, both in hydrostatic and nonhydrostatic regimes.

In the hydrostatic regime, study of 2D breaking mountain waves has shown that the mean flow is decelerated in the vertical between the ground and the theoretical breaking level, and uniformly in the horizontal. Tests with a GCM have indicated that the parameterization of the vertical flux of momentum is sufficient to accurately recover the deceleration existing in a meso-scale anelastic model. This study has also revealed the limitations of 2D simulations to investigate momentum transfers in orographic flows.

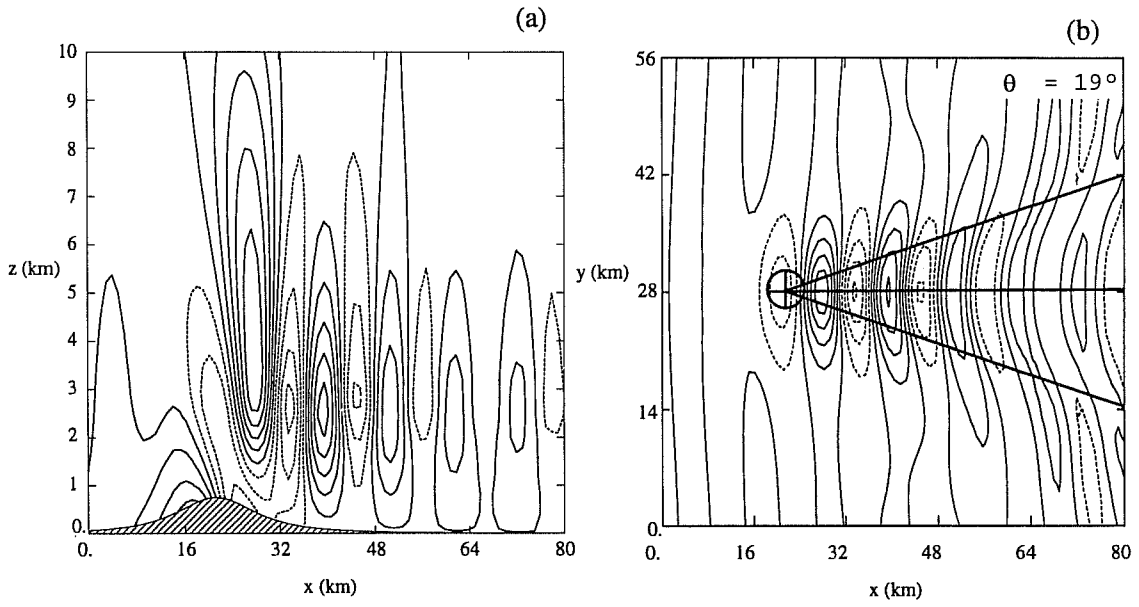

Figure 13: Meso-NH simulation of 3D trapped waves at $t^* = 30$: (a) vertical wind (contour interval .2 m s^{-1}) in a vertical section along the center plane. (b) Vertical wind (contour interval .2 m s^{-1}) at $z = 4h_0$ (negative values are plotted in dashed lines). The cross gives the obstacle position and heavy lines represent the theoretical wedge angle of the first transverse mode ($\theta_1 = 19°$).

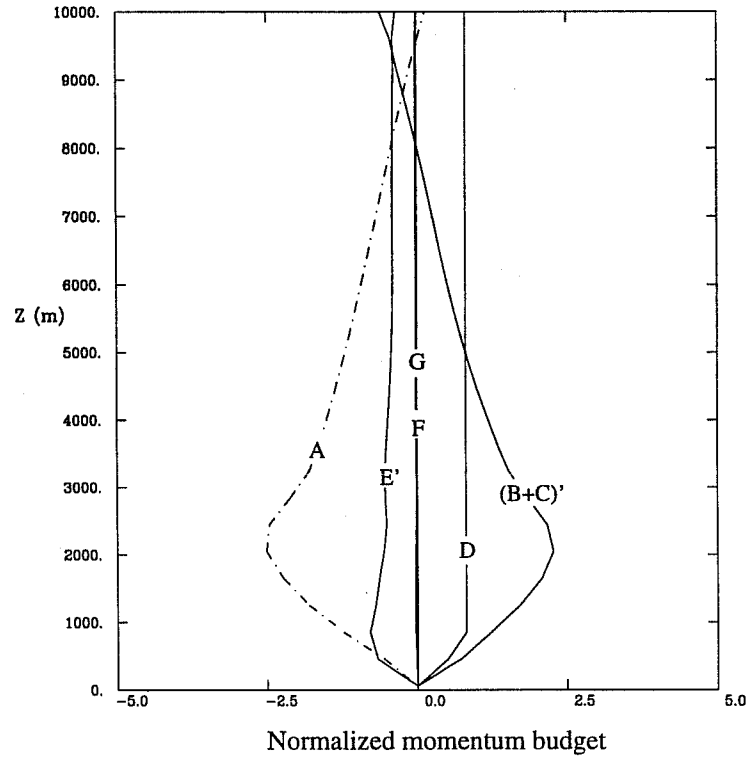

Figure 14: Meso-NH simulation of the 3D trapped waves case: time-averaged budget of $\rho_{ref} u$ in a ($6a$,$5a$) box centered on the obstacle. (a) Budget at $t^* = 30$. The time-average interval is set to $T^* = 3.4$, and the normalization factor is .025 $a\, h_0^2$.

In the regime of 3D quasi-symmetrical lee vortices, the mean flow is decelerated in a restricted region located near the wake. The analysis of lbc suggests that open conditions have no impact on the momentum budget in a 3D numerical domain, a significant difference with 2D numerical simulations. In the vortex-shedding regime, a very long model integration has shown the growth and the saturation of the perturbation after a very long time ($t^* = 160$). Concerning the momentum transfers, the vortex-shedding regime induces an increase of the mean-flow deceleration. An off-line test of a typical drag parameterization indicates that some adaptations would be required to improve the drag parameterization in a GCM, for this idealized flow where other momentum sinks (for instance surface friction) are ignored.

The investigation has been extended to the nonhydrostatic regime with a typical case of tlw. 2D tlw do not decelerate the large-scale flow at low levels, but significantly enhance the pressure drag, an effect which must be taken into account in drag parameterizations. Analysis of a typical case of 3D tlw leads to different conclusions than for the 2D regime: the mean flow is mainly decelerated in the low levels, below the region of stronger stratification. This deceleration may be caused by the decrease of the wave amplitude downstream of the obstacle (absent in 2D tlw) which prevents the transport of the deceleration far from the obstacle.

References

Bougeault, P. and P. Lacarrère, 1989: Parameterization of orography-induced turbulence in a meso-beta scale model. *Mon. Wea. Rev.*, **117**, 1870–1888.

Durran, D. R., 1995: Do breaking mountain waves decelerate the local mean flow? *J. Atmos. Sci.*, **52**, 4010–4032.

Eliassen, A. E. and E. Palm, 1960: On the transfer of energy in stationary mountain waves. *Geofys. Publ.*, **21**, 1–33.

Huerre, P. and A. M. Monkewitz, 1990: Local and global instabilities in spatially developing flows. *Ann. Rev. Fluid. Mech.*, **22**, 473–537.

Lafore, J. P., J. Stein, N. Asencio, P. Bougeault, V. Ducrocq, J. Duron, C. Fischer, P. Héreil, P. Mascart, J. P. Pinty, J. L. Redelsperger, E. Richard and J. Vilà-Guerau de Arellano, 1997: The Meso-NH atmospheric simulation system. Part I: Adiabatic formulation and control simulations. *Accepted for publication in Annales Geophysicae.*

Lott, F. and M. J. Miller, 1997: A new sub-grid scale orographic drag parametrization : its formulation and testing. *Quart. J. Roy. Meteor. Soc.*, **123**, 101–127.

Nance, L. B., 1995: On the relative importance of nonlinearity and mean flow variability in the generation of nonstationary trapped mountain lee waves. *PhD thesis*, 150 pp.

Phillips, D. S., 1984: Analytical surface pressure and drag for linear hydrostatic flow over three-dimensional elliptical mountains. *J. Atmos. Sci.*, **41**, 1073–1084.

Schär, C. and D. R. Durran, 1997: Vortex formation and vortex shedding in continuously stratified flows past isolated topography. *J. Atmos. Sci.*, **54**, 534–554.

Scorer, R. S., 1949: Theory of waves in the lee of mountains. *Tellus* 41–56.

Sharman, R. D. and M. G. Wurtele, 1983: Ship waves and lee waves. *J. Atmos. Sci.*, **40**, 396–427.